

The emergence of soft-glassy mechanics in simulated foams

Amruthesh Thirumalaiswamy,¹ Robert A. Riggleman,^{1,*} and John C. Crocker^{1,†}

¹*Department of Chemical and Biomolecular Engineering,
University of Pennsylvania, Philadelphia, Pennsylvania*

Several seemingly different soft materials, including foams, cells, and many complex fluids, exhibit remarkably similar rheological properties and microscopic dynamics, termed soft glassy mechanics. Here, we show that such behavior emerges from a simple model of a damped ripening foam, for sufficiently weak damping. In particular, we observe intermittent avalanche dynamics, bubble super-diffusion, and power-law rheology that vary as the damping factor is changed. In the limit of weak damping, the dynamics are determined by the tortuous low-lying portions of the energy landscape, as described in a recent study. For strong damping the viscous stresses cause the system configuration to evolve along higher energy paths, washing out small-scale tortuosity and producing motion with an increasingly ballistic character. Using a microrheological approach, the linear viscoelastic response of the model can be efficiently calculated. This resembles the power-law rheology expected for soft glassy mechanics, but unexpectedly, is only weakly sensitive to the damping parameter. Lastly, we study the reported memory effect in foams after large perturbations and find that the timescale of the memory goes to zero as the damping parameter vanishes, suggesting that the effect is due to viscous stress relaxation rather than slow structural changes stabilized by the energy landscape.

I. INTRODUCTION

Soft glassy materials (SGMs) [1–3] such as foams and emulsions exhibit complex physical and rheological properties that continue to defy explanation. Moreover, the similarity of soft glassy mechanics to that of living cells [4–6] and glassy materials [7] has long been noted. Previous experimental and theoretical models have captured different aspects of such systems while falling short of a complete physical picture. For foams, rheological experiments have shown conflicting results — showing weak [8, 9] or no [10] power-law frequency dependence of the dynamic shear modulus. Modeling efforts have largely focused on the now canonical ‘bubble model’ [11, 12], but the dynamic shear modulus of this model has not been reported. While a more recent study did report power-law rheology [13] it used a simplified system without damping. Further, experiments have shown memory effects [14, 15] in which a deformed foam shows perturbed mechanics which relaxes back to the unperturbed trend after a long time. The physical origin of this memory effect remains poorly understood.

Here, we study the soft glassy mechanics and rheology of foams, as well as their recovery from mechanical perturbation using a 3-D bubble model [11, 12, 16] with a simple damping law [7, 12], driven by simulated Ostwald ripening [17]. Previous stress-strain simulations [16, 18] of a 2-D bubble model without ripening have indicated a transition to avalanche dynamics with reduced applied strain rate. We look for a similar effect in our ripening foam model by changing the damping parameter ξ , effectively changing the relative rates of ripening

and viscous relaxation. This however requires the computationally expensive integration of the bubble model’s equation of motion at low ξ . We find that for sufficiently low damping (or equivalently slow ripening), the system dynamics are determined by the tortuous character of the energy landscape, as observed in a damping-free model [13], leading to avalanches in energy, super-diffusive bubble motion, and fractal configuration-space paths. For stronger damping, this behavior disappears, being replaced by a more continuous motion having a ballistic character. We use a microrheological approach to determine the dynamic shear modulus of our model from its intrinsic, non-thermal fluctuations [19, 20], and find that it generically has power-law rheology resembling recent experimental measurements [8, 9]. The rheology exponent is, unexpectedly, only a weak function of damping, providing new insights into the origin of power-law rheology in SGMs. Lastly, we study foam’s recovery from mechanical perturbation by randomly scrambling the locations of bubbles in our model, finding that scrambling leads to perturbed mechanics that slowly return to the (average) unperturbed baseline, resembling experimental reports of mechanical memory in foams [14, 15]. The foam recovers to the baseline more quickly as the damping factor is reduced, and does so immediately when damping is removed, indicating that the memory effect is controlled by viscous stress relaxation, and not due to activation between energy minima.

II. DAMPED SGM MODEL

A. Coarsening bubble dynamics

We model a coarsening foam using the bubble model [11, 12] with a simplified damping rule and simulated Ostwald ripening. While the bubble model has been tra-

* rrig@seas.upenn.edu

† jcrocker@seas.upenn.edu

ditionally used to simulate foams [11, 18], it also serves as an effective model for many other SGMs [7, 13, 21]. The constituent bubbles of foam in this model are treated as soft-sphere particles that can overlap and interact via a pairwise repulsive potential when overlapping:

$$V(\mathbf{r}_{ij}) = \begin{cases} \frac{\epsilon}{2} \left(1 - \frac{\|\mathbf{r}_{ij}\|}{a_i + a_j}\right)^2, & \text{if } \|\mathbf{r}_{ij}\| < a_i + a_j \\ 0, & \text{otherwise.} \end{cases} \quad (1)$$

with r_{ij} being the distance between two bubbles of radii a_i and a_j , and $V(\mathbf{r}_{ij})$ being the corresponding potential.

The positions of the bubbles interacting via the pairwise potential in Eq. 1 are evolved using an (over-damped) equation of motion [11]. Notably, we consider a simplified version of the viscous force, $\mathbf{F}_i = \xi \mathbf{v}_i$ [7, 12], on each bubble to reduce computational overload while preserving relevant model physics.

$$\xi \frac{d\mathbf{r}_i}{dt} = - \sum_j^{nn} \frac{\partial V(r_{ij})}{\partial r_i} \quad (2)$$

with the right-hand side representing a summation over neighboring bubbles that contribute to the force on bubble i . Meanwhile, the left side is the damping force with ξ being the effective viscous damping factor.

To simulate the mass exchange between bubbles due to Ostwald ripening [17], the bubble radii are allowed to evolve while keeping total bubble volume constant (preserving notional mass). Ripening causes larger bubbles to grow and smaller ones to shrink over time via a pairwise mass flux. We model this process with a flow rate that depends on the degree of overlap between neighboring bubbles (over the overlap cross-section), along with a mean-field flux that flows through the connected phase medium.

$$Q_i = \underbrace{-\alpha_1 \rho \sum_j^{nn} \left(\frac{1}{a_i} - \frac{1}{a_j}\right) A_{\text{overlap}}}_{\text{neighbor-neighbor}} \quad (3) \\ \underbrace{-\alpha_2 \rho \left(\frac{1}{a_i} - \frac{1}{\langle a \rangle}\right) a_i}_{\text{mean-field}}$$

As indicated, the first term represents the pair-wise mass-flux between neighboring bubbles over the cross-section of overlap and the second represents the mean field contribution. The values for $\alpha_1 (= 0.05)$ and $\alpha_2 (= 0.002)$ were chosen akin to our previous study [13]. When a bubble's volume turns negative over the course of the simulation, we remove it from the simulation box, while ensuring that the mass of the deleted bubble and its neighbors is conserved.

To realize the overall evolution of the system, we independently evolve the system using the equation of motion (Eq. 2) and ripening rules (Eq. 3) for all bubbles at every time step. We use a simple explicit Euler scheme with small dt values, to numerically integrate the equations of motion (more details in Appendix A 2). The use of other integrators like a second-order Runge-Kutta numerical discretization led to similar results. While we note that the equations of motion can be physically unstable at very high energies (when there is a significant overlap between bubbles), we verify that such large overlaps are not present at the energy levels presented here. Further, while using small step-sizes within the range of numerical stability (more details in Appendix A 2), we ensure the simulation has converged by cross-validating with smaller step-sizes (dt). It may be noted here that smaller step-sizes (dt) are required for lower values of ξ , and thus are computationally more expensive to simulate.

Bubble model simulations [13] when initialized randomly, eventually reach a dynamic steady state with a characteristic bubble size distribution and various systematic trends in properties such as total energy or mean bubbles size, as with experiments [22]. We initialize a system of $N \sim 1000$ bubbles at a volume fraction of $\phi = 0.75$ (just above its jamming volume fraction [13, 23]) with a Weibull bubble radius distribution, $\mathbf{P}(a) \sim (k/\lambda)(a/\lambda)^{k-1}$, where $k = 1.75$, $\lambda = 0.73$, and let the system evolve as a function of time. This distribution is representative of the steady state bubble size distribution that a Gaussian initialized system reaches when evolved in the quasi-static limit ($\xi \rightarrow 0$) [13]. Using this as a starting point for all our simulations, we model over a range of damping factors (ξ) and calculate various physical quantities of interest. It must be noted that we end our simulations when bubbles grow considerably large leading to multiple (> 1) overlaps between 2 bubbles. This happens much earlier in larger ξ systems thus producing shorter simulation trajectories overall.

Fluctuations in the system's total potential energy change significantly for different simulated viscosities. Two distinct limits are observed, as shown in Fig. 1. Low viscosity simulations ($\xi \leq 0.001$), produce large fluctuations in $\Delta U(\Delta t = 1)/U(t)$ (see Fig. 1a, indicative of avalanche, intermittent dynamics). These are suggestive of the system following the 'bumpy' lower levels of the energy landscape. Conversely, with higher ξ values, the system no longer moves from minimum to minimum of the underlying energy landscape but evolves in a dynamic force balance between the larger interaction forces and viscous stresses. This allows the system to fly over the barriers and rugged features of the energy landscape, with a higher time average potential energy for the system (see Fig. 6a). This change in the fluctuations is shown more clearly in the distribution of energy drops, Fig. 1b, which becomes more heavy-tailed at lower ξ . Further, a similar trend can also be seen in Fig. 1c, where the average coordination number (over a system configuration) is higher at higher viscosities, indicating

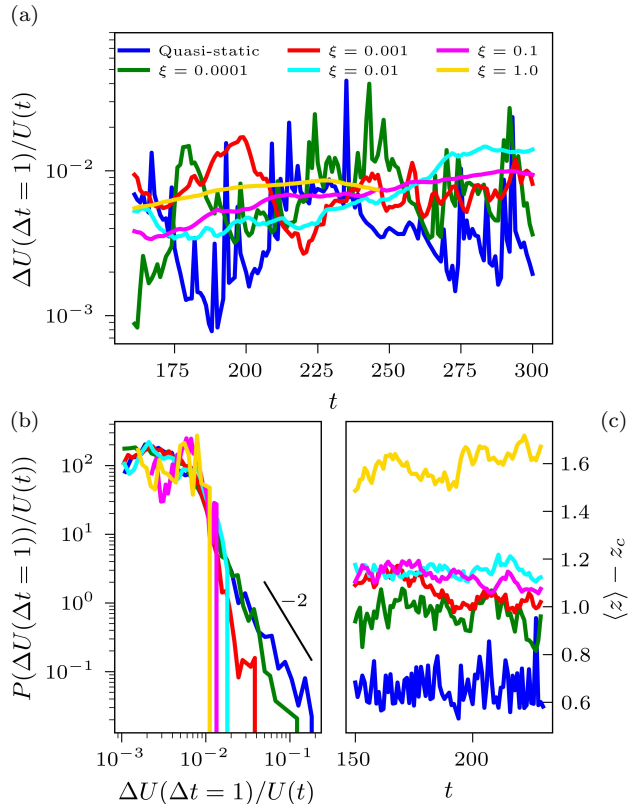


FIG. 1. (a) Traces of relative energy differences $\Delta U/U(t)$ for $\Delta t = 1$ or simulation points spaced by 1 time unit) are sensitive to intermittent dynamics. For lower damping, $\xi \lesssim 0.01$, the relative change in energy shows abrupt peaks characteristic of intermittent motion. (b) Lower ξ simulations show a heavy-tailed probability distribution of energy fluctuations, typical of an avalanche system. As the system becomes more viscous, the energy fluctuations become more Gaussian. (c) The average system coordination number $\langle z \rangle$ remains low for lower ξ simulations, characteristic of lower energy configurations close to potential energy minima on the landscape. z_c is the critical coordination for jamming, with $z_c = 6$ in $3-D$ [21].

that viscous stresses are shifting the foam structure away from the minimum energy states, and farther from jamming, defined as coordination with $\langle z \rangle \simeq z_c$ [21]. Thus foam configurations formed at low damping explore lower and more tortuous portions of the energy landscape and ones with higher damping cruise through higher and apparently smoother portions of the energy landscape.

To characterize the system's high dimensional motion over the energy landscape, we look at the path traversed by the system through configuration space for the range of viscosities studied. The different time points on a simulation trajectory in configuration space are analyzed for end-to-end distances (ΔR^2) and path contour lengths (Δs). This serves as a measure of the tortuosity of the $3N$ dimensional configurational trajectory taken by the system over time. As expected from our conclusions above, we observe that lower viscosities yield fractal, self-similar

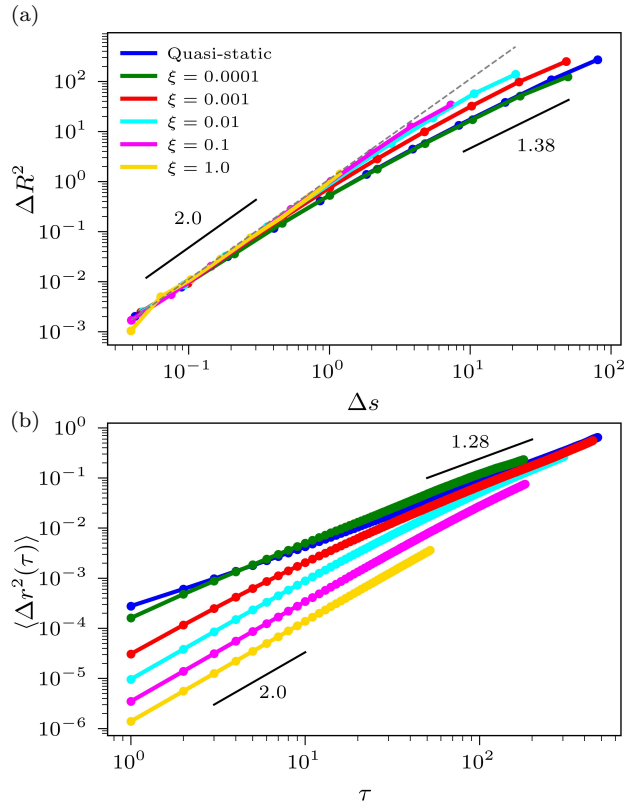


FIG. 2. Analysis of bubble motion in $3-N$ dimensional space and real space shows a mixture of fractal and ballistic motion. (a) The different simulation points in high dimensional ($3N$) space are analyzed for end-to-end distances ΔR^2 and contour lengths Δs to study fractal scaling over different length scales. Simulations with larger ξ values give almost ballistic scaling in hyperspace. However, lower ξ lead to a more tortuous trajectory characteristic of a fractal path, leading to super-diffusive scaling. The grey dashed line is a reference with ballistic scaling $\Delta R^2 \sim \Delta s$ throughout. All data points above represent values pooled over 4 simulations and log-bin-averaged over contour distances. (b) Time and ensemble (4) averaged mean-squared displacement for an ensemble of bubbles that remain finite sized throughout our simulations, plotted for the different ξ values shows ballistic motion rolling over to a super-diffusive form for lower ξ simulations. In comparison, more viscous simulations show more ballistic behavior over a larger range of τ .

scaling at large lengthscales with a fractal dimension of $D_f \sim 2/1.38$ (slope at large distances) $\simeq 1.45$ (see Fig. 2a) – capturing the intrinsic fractal physics of the landscape [13]. Simulations with higher damping show almost no large lengthscales fractal character, indicative of their ability to avoid lower energy portions of the energy landscape. Alternatively, the slight bends on Fig. 2 may be interpreted as a shift in the lengthscales (as a function of ξ) over which a fractal slope would be observed. This, however, is further evidence for the self-similar fractal nature of the landscape and indicates that one would have to examine considerable lag times (or configuration

distances traveled by the system) to observe soft-glassy mechanics for systems with larger damping. Here, it must be noted that when particles shrink to zero size as a result of ripening, we fix their positions in space, thus conserving the number of dimensions ($3N$) used to calculate ΔR^2 . In Fig. 2b, we compute the ensemble and time-averaged mean-squared displacement as a function of lag time (τ). These curves show a functional form that is similar to that of the ΔR^2 above because the mean-squared displacement is a projection of those curves to 3-D space; the slight difference in the exponent is due to the calculation being done on a slightly different ensemble of bubbles that remain finite sized throughout the simulation.

Here, one may also identify a dimensionless group of interest called the *Deborah number* De , which can be expressed as the ratio of time scales associated with relaxation and the mode of driving—the two relevant dynamic processes for this system. Here, that would be the damped relaxation time from Eq. 2 ($\tau_R = \xi \langle a \rangle^2 / \epsilon$) and timescale associated with changing bubble radii (a) imparted by the ripening process, Eq. 3 ($\tau_C = \langle a \rangle^2 / \alpha_1$ when $\alpha_1 > \alpha_2$). This gives us a *ripening Deborah number*, ($De_\alpha = \xi \alpha_1 / \epsilon$) which is a ratio of the relaxation (τ_R) and coarsening (τ_C) times (typically ranging between $10^{-3} - 10^{-6}$ for our simulations). This dimensionless group presumably depends on the system's volume fraction ϕ and its proximity to the jamming volume fraction ϕ_J [11, 18].

This dimensionless group formalism can be a useful way to explain many previous experimental and simulation results [12, 16, 18]. We begin by noting that the avalanche dynamics and intermittent rearrangements observed in our simulations resemble previous studies of similar systems [11] driven by shear strain instead of coarsening. Various comprehensive studies [16, 18] using $2D$ shear strain point out a similar transition to avalanche rearrangement events below a certain shear strain rate. Thus, our results can be interpreted as a transition in landscape physics as a function of De_α while shear simulation results [16] can be explained using a corresponding *shear Deborah number*, De_γ .

For a foam experiment, we note that the energy scale and damping factor vary as the system evolves: $\epsilon \simeq \sigma \langle a \rangle^2$ [11] and $\xi \propto \langle a \rangle$, while α_1 is effectively independent of $\langle a \rangle$. Thus experimentally, $De_\alpha \propto \langle a \rangle^3$ changes for dynamically aging foam where $\langle a \rangle$ increases as a function of time [13, 22] (see Fig. 5). This keeps pushing the aging system away from the landscape-dominated regime, potentially explaining the issue associated with the shifting cut-off [1], and tending to produce behavior akin to high ξ simulations.

B. Rheology of SGMs

The rheology of soft-glassy systems is typically found to be weakly frequency dependent (solid-like), often with

a power-law form, while different experiments on foams [8, 10] yield apparently conflicting results. Computationally, capturing low-frequency responses to applied strains can be very expensive, making the determination of rheology difficult [13]. Here, we provide a numerical procedure that derives its essentials from a microrheological approach [19, 24] that computes the power spectra of the active, fluctuating shear strain and stress from the particle motions, and computes the dynamic shear modulus from their ratio.

We begin by noting that one can relate the stress ($\sigma(t)$) and strain ($\gamma(t)$) to the creep compliance ($\mathbf{J}(t)$) using the theory of linear response [25, 26] and the Boltzmann superposition principle, relating them through a convolution:

$$\begin{aligned} \mathbf{J}(t) \otimes \dot{\sigma}(t) &= \gamma(t) \\ \int_{-\infty}^t \mathbf{J}(t-t') \dot{\sigma}(t') dt' &= \gamma(t) \end{aligned} \quad (4)$$

While this basic constitutive equation represents the relation between the macroscopic stress and strain for a linear material, we extend this formalism to its microrheological version wherein each bubble/particle can be treated as a tracer moving in a homogeneous viscoelastic continuum (formed by all the other bubbles) driven by active fluctuating stresses. Thus, typically one can use the bubbles' positional vectors describing their motion in the effective medium to describe the local, time-dependent strain in the effective medium [24]. Similarly, the local fluctuating active stress acting on each bubble in the system can be computed as follows [27, 28]:

$$\sigma(\mathbf{r}_i) = - \left(\sum_j^{nn} \mathbf{r}_{ij} \otimes \mathbf{F}_{ij} \right) \delta(\mathbf{r} - \mathbf{r}_i) \quad (5)$$

where r_{ij} and F_{ij} represent the inter-particle displacements and forces between particles i and j .

Applying the above equations directly to the data would be impractical because the $\sigma(t)$ and $\gamma(t)$ signals for each bubble are random functions of time. Instead, we transform the equation described in Appendix B 1 to a relation between the ensemble-averaged mean squared differences (MSD), the stress, and strain. The stress MSD is calculated by considering the squared difference between the three off-diagonal elements of the bubble-wise symmetric tensor (see Eq. 5). Further, we consider the ensemble average over all bubbles in our system and over similar lag times to get a statistically consistent MSD. Meanwhile, the strain MSD can be estimated using the positional MSD or mean-squared displacement introduced earlier (see Fig. 2a). These quantities can further be related using the modified Fourier transformed (FT) version of the above equation [13, 19, 20]:

$$|G^*(\omega)|^2 \simeq \frac{\widetilde{\Delta\sigma^2}(\omega)}{3\pi \langle a \rangle \overline{\Delta\mathbf{r}^2}(\omega)} \quad (6)$$

To avoid assumptions and approximations related to computing Fourier transforms of these MSDs over a finite range of lag times, [13, 20], we consider the exact convolutional relation described in Appendix B 1. This equation can be further modified using the Wiener-Khinchin theorem and the relationship between autocorrelation and MSD for the stress and strain, giving us the following equation:

$$\begin{aligned} 2J^2(0)\langle\sigma^2\rangle + \int_0^{\tau_i} f(\tau_i - t')(\langle\sigma^2\rangle - \langle\Delta\sigma^2\rangle(t')/2)dt' \\ = (\langle\gamma^2\rangle - \langle\Delta\gamma^2\rangle(\tau_i)/2) \\ \simeq 3\pi\langle a \rangle(\langle\mathbf{r}^2\rangle - \langle\Delta\mathbf{r}^2\rangle(\tau_i)/2)/\langle a \rangle^3 \quad (7) \end{aligned}$$

where $f(\tau_i)$ is defined as follows,

$$f(\tau_i) = \left(\int_0^{\tau_i} \dot{J}(\tau_i - t'')\dot{J}(t'')dt'' + 2J(0)\dot{J}(\tau_i) \right)$$

where $\Delta\sigma^2(\tau)$ and $\Delta\gamma^2(\tau)$ represent the time-averaged, mean-squared difference of the bubbles' stress and strains, in our analyses. We approximate the strain using the position vector, \mathbf{r} [19, 24] as discussed above. Further, we ensemble average our MSDs over 4 simulation runs. Finally, to represent the creep compliance, we use a modified version of the model suggested by Lavergne and co-authors in Ref. [8]: $J(t) = 1/G_\infty + k_D/G_\infty[(1+t/\tau_0)^\beta - 1]$ (more details in Appendix B 2). Using this as a model for the viscoelastic rheology for the foam, we undertake a simultaneous fitting operation for the parameters of the model, i.e., G_∞, k_D and β , at various lag times or τ_i in the convolutional integral equation shown above (Eq. 7). Using the optimal parameters from the fit gives us the creep compliance and, subsequently, the complex modulus $G^*(\omega)$ using the relation, $G^*(\omega)J(\omega) = 1/i\omega$. Further details of the derivation and mathematics of the numerical procedure are provided in Appendix B 1. It may be further noted that attempts to model the rheology using a Maxwell model produced inferior solutions to Eq. 7, with the power-law model cited above providing significantly better fits.

The results from the computed creep compliance and dynamic shear moduli are summarized in Fig. 3. $G^*(\omega)$ exhibits a power-law regime over the ω range of interest and is characteristic of behavior predicted in theory [1], simulations [13] and observed in experiments [8–10]. Recent experiments and our simulation results here (see Fig. 3), evaluated with a robust numerical approach provide clear evidence in support of the existence of power-law rheology in SGMs. Fig. 3a, shows the fits for the $J(t)$ model described above, with a family of curves with similar power-law exponents. Considering the semi-analytical FT to obtain $G^*(\omega)$ gives us the viscoelastic moduli with

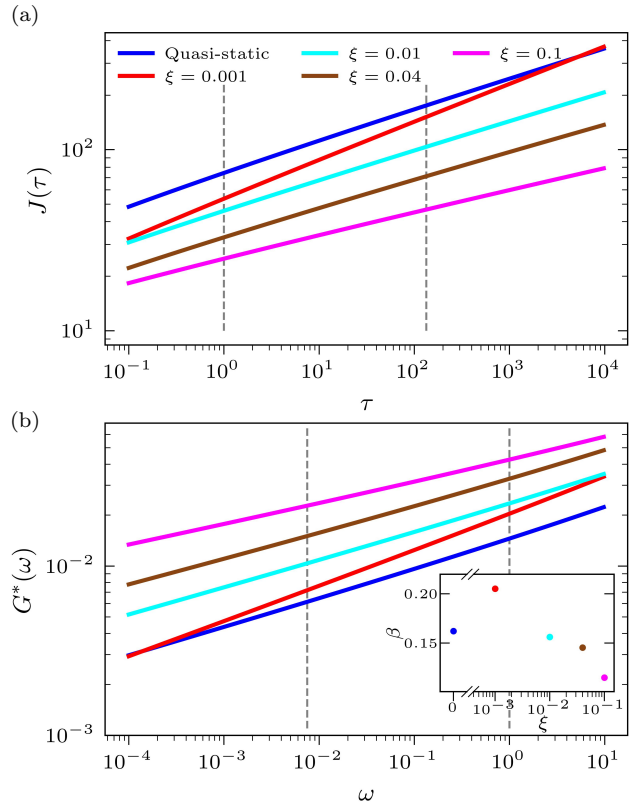


FIG. 3. We compute the viscoelastic moduli for the dynamic viscous simulations considered from the fluctuating stresses and displacements of bubbles in the simulation, as described in the text. ξ values with data over a significant τ range were considered for the calculation. The dotted grey lines indicate the τ range of the MSD data used for the above calculation. (a) Fitting the model explained in the text to simulation data gives us suitable fits with a family of curves with power-law behavior. The creep compliance scales as $J(\tau) \sim t^\beta$ in the lag time range shown above. (b) $G^*(\omega)$ obtained from $J(\tau)$, gives us power-law rheology in ω i.e., $G^*(\omega) \sim \omega^\beta$. This behavior is observed at all ξ values calculated above. (inset) The predicted β values, indicative of the log-slope for the curves in (b), hover consistently in the range $\sim 0.15 - 0.2$, similar to previously observed values in simulation [13], and experiments [8, 9].

a power regime defined by $G^*(\omega) \sim \omega^\beta$, with weak dependence of the exponent β on damping, showing that this is a universal feature for foams, regardless of ξ damping.

C. Memory and recovery in perturbed SGMs

The SGM system shows a significant downhill descent in energy as the largest bubbles coarsen and grow. As this downward trend continues, the system reaches a dynamical scaling steady state [13]. While it is unclear whether configurations in this regime form an ergodic ensemble over some characteristic time, the bubbles show stable trends in various structural quantities like average co-

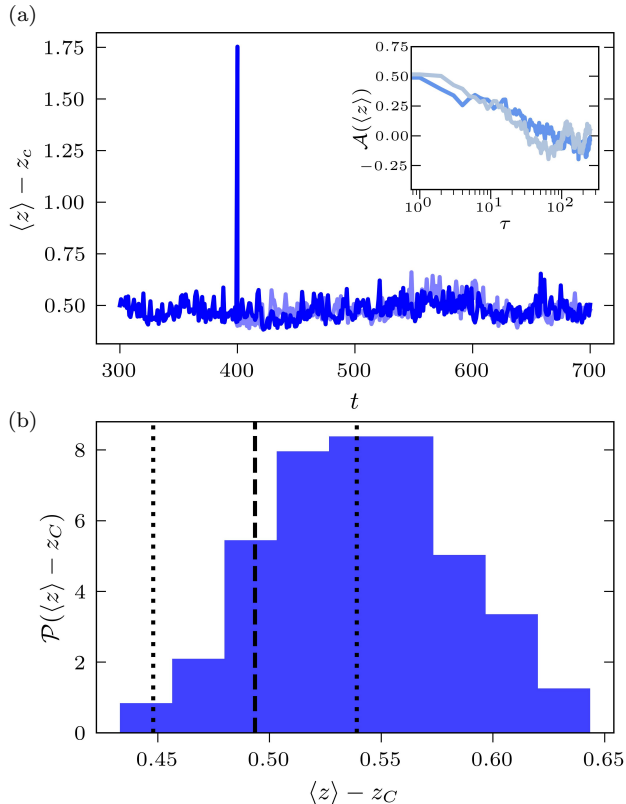


FIG. 4. Scrambling a quasi-static system shows an immediate return to trend. (a) We scramble the configurational positions of a system in steady state (at $t = 400$) in a quasi-static ($\xi = 0$) simulation. Surprisingly, the system always finds a ‘new’ steady state right away, as indicated by the coordination number ($z - z_C$) measured here, and continues to evolve with similar dynamic properties. The dark and light symbols represent the scrambled and unscrambled simulation, respectively. (b) Running multiple (~ 100) such scrambles at $t = 400$, gives us a Gaussian distribution of $\langle z \rangle$ as shown above. This overlaps well with $\langle z \rangle$ values obtained at $t = 400$ for 10 different realizations of the same simulation as indicated by the mean \pm standard deviations. This tells us that the scrambled simulation returns to the newly found steady state instantaneously. (inset) Moreover, the temporal autocorrelations for these z ensembles - scrambled and unscrambled - provide similar decorrelation times. These findings indicate similar dynamic properties for the scrambled and unscrambled simulation.

ordination number, mean bubble radius, normalized radial distribution, etc. Bubbles initially move around to reach the steady state, defined by the dynamical scaling ‘attractor’ on the energy landscape, and then continue to evolve in this steady state ensemble. Any perturbation away from the attractor would thus lead the system back to a ‘new’ steady state as defined by the structural and dynamical properties of the attractor and the system landscape. Experiments have observed [14, 15] that a strain-perturbed foam relaxed back to its unperturbed steady state after an unexpectedly long waiting time, and

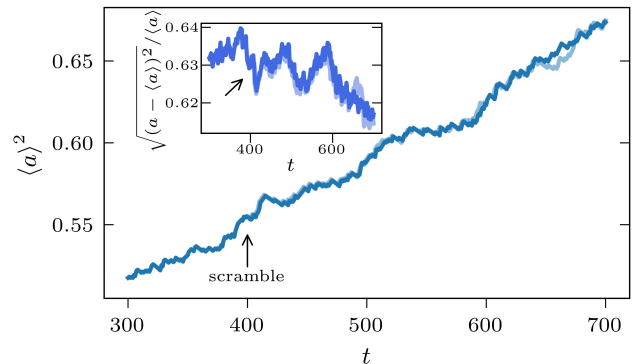


FIG. 5. Scrambling a quasi-static system shows no change to ripening evolution. Here, we look at the structure through the radial distribution formed at steady state for a scrambled and unscrambled system. As previously in Fig. 4, the system instantaneously continues in steady state. As can be noticed, the slope changes for the scrambled simulation at $t = 400$ (indicated by arrows), indicative of a new foam initiation time [13]; however, the trend remains linear, consistent with dynamic scaling state behavior $\langle a \rangle^2 \sim t_{\text{age}}$.

have described this as a memory phenomenon or measure of history dependence. The consensus [14, 15] on the origin of this memory is that coarsening mediated excitations are needed to enable the system to overcome local minima that the perturbed system relaxes into. Thus, the long waiting time has been considered a result of slow coarsening.

To study this phenomenon’s structural and dynamical significance computationally, we run a set of simulations using our modified damped model over various ξ values. We consider the theoretical extreme of a perturbation by introducing positional scrambles in our system. To do so, we begin with a typical steady-state system and randomly scramble the various $3N$ positions of the bubbles. This scramble randomly assigns a point in hyperspace for the system of soft spheres, providing a random structural perturbation. We then continue with the relaxation-coarsening procedure described previously in Section II A. It must be noted here that for the quasi-static case when $\xi = 0$, we relax the system to its first energy minimum (i.e. mechanical equilibrium) using FIRE [29] instead of using Eq. 2.

For the quasi-static case, we see that the system, upon one (or even multiple) scrambles, returns to the earlier dynamical scaling steady trend (see Fig. 4a) immediately. Indicators like $\langle z \rangle$ and $\langle a \rangle^2$ show no significant change from steady-state behavior, as can be seen in Fig. 4 which plots the scrambled (at $t = 400$) and unscrambled average coordination number as a function of time. Here the scrambled system experiences no barriers to reaching this ‘new’ steady state with FIRE traversing the large configurational distance on a relatively smooth portion of the energy landscape (at higher energies) to find the nearest (primary) minima. It may be noted that the scramble

moves the system to a random $3N$ -dimensional configuration on the energy landscape. The system thus evolves in the particular meta-basin corresponding to the scrambled positions going forward. So while a single simulation might not ergodically explore all portions in configuration space, these different hyperspaces on the energy landscape have similar structural properties. Small changes in moving ensemble averages indicate the slight variations in different regions or metabasins of the energy landscape. Effectively, all these primary minima that the minimizer finds belong to the 'steady-state ensemble' of the particular foam radii distribution realization at $t = 400$.

To test whether the scrambled simulation actually returns to the 'steady-state ensemble' for a similar foam at the same age, we compare the average coordination numbers at $t = 400$ for 10 different quasi-static simulations (different positional initializations at $t = 0$) in Fig. 4b; with a pool of coordination numbers obtained from scrambling the same test simulation (from Fig. 4a) configuration at $t = 400$, a 100 different ways and quenching them using FIRE. As seen in Fig. 4b, the distribution of average coordination numbers for a quenched minima from the test simulation lies in the range of expected steady-state $\langle z \rangle$ values for a similar foam simulation at the same age. Lastly, looking at the inherent temporal correlations in the coordination number further tells us that similar correlations get rebuilt after the system evolves on the randomly chosen 'metabasin' on the energy landscape Fig. 4a(inset). Thus we conclude that while the system doesn't return to the exact configurational hyperspace on the energy landscape, the foam exhibits a 'memory' effect in various physical and dynamical properties.

Interestingly, this also doesn't affect the coarsening mediated bubble size distribution reached at dynamic scaling as seen in Fig. 5. This can be seen in the average system radii measured over time in Fig. 5. While there is a noticeable change in the rate of radial change or the slope, the trajectory remains in steady state as indicated by the linear gradient. Additionally, the scrambled simulation continues to evolve with similar moments of the radii distribution (see Fig. 4a(inset)). Overall, this shows that while any steady state structure built in by the dynamics and coarsening before the scramble gets ruined by the perturbation, it gets restored immediately by quenching to the nearest minima (using FIRE).

Repeating the same computational experiment at finite ξ provides insight into the mechanism of the memory phenomenon. In agreement with previous experiments [10, 15], we see that the system requires a surprisingly long time to recover to its former steady state trend (see Fig. 6). However, unlike previous suggestions of this time-scale being coarsening-mediated, we observe a ξ dependent phenomenon. This viscous time scale dictates the time the system takes to relax any energetic stress built in by the overlaps caused by the positional scramble. Larger ξ leads to a longer time for the sys-

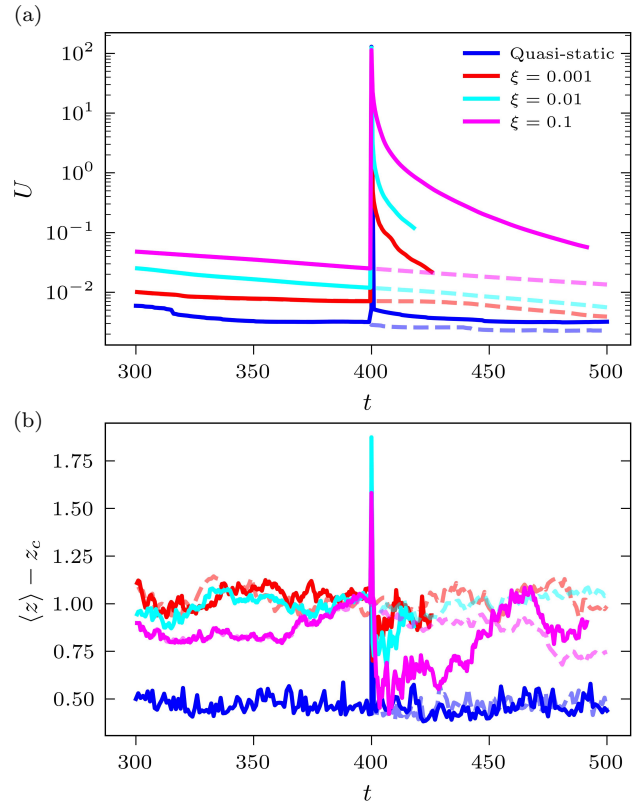


FIG. 6. Scrambled foams with damping show very slow relaxation towards their prior trends in energy and coordination. Finite ξ simulations are scrambled at $t = 400$ and evolved using the dynamical equation Eq. 2. (a) The potential energies post scrambling show a progressive trend in reaching the steady state. Fitting the energies (b) The mean coordination number $\langle z \rangle$ of the system shows similar ξ dependent trends. Interestingly, the initial dynamics directs the system to lower $\langle z \rangle$ configurations before relaxing to the appropriate steady-state value.

tem to relax these unstable overlaps. Fig. 6 shows the progression of energy and average coordination number towards equilibrium after a positional scramble. Interestingly, the z values shoot below the steady state line post scramble before trending back to steady state, much like previous experiments measuring rearrangement rate [14]. Finally, one may note here that while the waiting times seem to be damping dependent, they are, however, much larger than $\tau_R = \xi \langle a \rangle / \epsilon \sim \mathcal{O}(\xi)$. This discrepancy might be due to the extreme nature of positional perturbation introduced in our simulation – which introduces many large and small perturbations for all N bubbles away from the nearest steady-state ensemble configuration. Thus, the waiting time is a compounded sum of all these different distances that the bubbles must traverse to reach the 'new' steady state.

III. CONCLUSIONS

We have shown that the ‘bubble model’ with simple damping and simulated ripening recreates many of the exciting phenomena reported for soft-glassy materials. Specifically, this model exhibits avalanche, intermittent dynamics at low viscosities with non-Brownian super-diffusive motion. Considered in high-dimensional configuration space, such motion occurs along a fractal configurational path that is constrained to the lowest energy portions of the potential energy landscape. We find that the energy minima of the bubble model are clustered together in configuration space, scattered along the configuration path followed by the model (at low viscosity). In the practical absence of viscous stresses, the system hops from each (ripening destabilized) energy minimum to a nearby, adjacent energy minimum. This landscape-dominated motion subsequently produces the observed super-diffusive motion and stress and strain fluctuations corresponding to power-law rheology. As the simulated viscosity is increased, the system shows progressively smoother dynamics and motion with a more ballistic character. In this case, viscous stresses cause the configuration never to explore the true potential energy minima but instead evolve along a path that is adjacent to the cluster of energy minima. The system effectively stays at higher potential energy, and the finer details of the fractal configuration path seen at lower viscosity are washed out, leading to a straighter path and more ballistic motion. Between these two limits, one can find a gradation of properties, where the system displays increasing characteristic length and time scales above which the low viscosity behavior may still be observed.

This model also successfully generates power-law rheology, which previously has not been reported for a damped bubble model. However, unlike other properties, power-law rheology seems to be a consistent feature in SGMs over a wide range of viscosity values. This suggests an extended fractal nature for the energy landscape, consistently producing power-law rheology even when the configurations are at energy somewhat above the energy minima. Further, our microrheology-based approach provides a robust and reliable way to compute viscoelastic moduli from force and strain fluctuations measurements of constituent particles and is free of any systematic truncation errors associated with earlier microrheological methods.

Lastly, we investigate the ‘memory’ of the ripening bubble model for mechanical perturbations by randomly scrambling the bubble positions. We find that scrambled configurations (effectively a random point in configuration space) must relax a long configuration distance before reaching their first potential energy minimum. Moreover, those first energy minima are indistinguishable (statistically) from the ensemble of configurations explored by other ripening simulations of the same age. This is most clearly shown by the quasi-static simulation that immediately recovers its earlier (ensemble averaged)

baseline properties when it reaches its first energy minimum. For finite viscosity, the system can take a long time to traverse the required configuration distance to return to the vicinity of the energy minima cluster and recover its earlier mechanical properties. In viscous systems, this recovery time (and effective ‘memory’ time) is proportional to the viscous relaxation time of the model. This viscosity-mediated recovery process is contrary to previous experimental inferences and a consequence of the barrier-free potential energy landscape at higher energies that the perturbed system must traverse.

Future work would include developing a model that captures other long-time characteristics of these SGMs. We hope that such a description will provide a more complete and practical model for SGMs. Modeling the physical properties of the many materials categorized under SGMs could be of potential use in fields ranging from material science (foams and complex fluids) to biology (living cells [4, 5]).

AUTHOR CONTRIBUTIONS

A.T., R.A.R., and J.C.C. designed research; A.T. performed research and analyzed data; A.T., R.A.R., and J.C.C. wrote the paper. R.A.R. and J.C.C. contributed equally to this work.

ACKNOWLEDGMENTS

We are grateful for valuable conversations with Douglas Durian, François Lavergne, Andrea Liu, Talid Sinno, and Véronique Trappe. This work was supported by NSF-DMR 1609525 and 1720530 and computational resources provided by XSEDE through TG-DMR150034.

Appendix A: Damped SGM Model

1. Underdamped limit of an overdamped equation

The equation used for the simulations, as described in the main text, is:

$$\begin{aligned} \xi \frac{d\mathbf{r}_i}{dt} &= \mathbf{F}_i \\ &= - \sum_j \frac{\partial V(r_{ij})}{\partial \mathbf{r}_i} \end{aligned} \quad (\text{A1})$$

It can be seen that the equation is similar to an overdamped equation of motion. However, it must be noted that though the equation resembles and has the characteristics of an overdamped equation of motion, the same is not due to a large viscosity but rather the non-inertial

nature of the constituent particles considered in the system. One may recall that dynamics for a mass attached to a damped spring are mediated by the damping factor $\zeta = b/(2\sqrt{km})$. That can be evaluated for our system of interest as follows $\zeta \simeq \xi/\sqrt{\epsilon\rho\langle a \rangle}$. Since overdamped dynamics is achieved when $\zeta \geq 1$, we see that the non-inertial particles ($\rho \rightarrow 0$) in our case give rise to the so-called overdamped equation of motion. Meanwhile, we continue to operate with a finite value of ξ .

2. Integration and stability

The simulation can be summarized as a numerical integration of the two equations – Eq. 2 and eq. 3 using a numerical integration technique. Due to the stiff nature of Eq. 2 (especially at small ξ values, one needs to choose appropriate dt values to ensure any error perturbations don't diverge as the simulation proceeds and that the solution is a converged one. We use a simple Explicit Euler scheme to perform our integration here. We note that other methods, like implicit Euler and second-order Runge Kutta scheme, provide more extensive stability regimes for dt and are more accurate but can have more significant computational overload associated with the integration scheme. Below, we perform a simple numerical stability test.

We start by considering Eq. 2 for all N particles or $3N$ degrees of freedom, i.e., $i \in \{1, 2, \dots, 3N\}$, which can be expressed in terms of the Hessian for using a Taylor expansion as follows: and

$$\begin{aligned} \xi \frac{d\mathbf{r}}{dt} &= \mathbf{F} \\ &= \mathbf{F}_0 - \mathbf{H}\mathbf{r} \end{aligned} \quad (\text{A2})$$

where \mathbf{r} , \mathbf{F} are $3N$ dimensional vectors and \mathbf{H} is a $3N \times 3N$ matrix or the Hessian of the potential field. We may note here that for most ξ simulations, the system configurations are close to mechanical equilibrium, so for our stability analysis, we may approximate this using $\mathbf{F}_0 \simeq 0$. Further one may note that the any error ϵ_i would propagate via an equation similar to Eq. A2:

$$\xi \frac{d\epsilon}{dt} = -\mathbf{H}\epsilon \quad (\text{A3})$$

Now, using the Explicit Euler formalism, for time steps $n+1$ and n , we get:

$$\begin{aligned} \xi \frac{\epsilon_{n+1} - \epsilon_n}{dt} &= -\mathbf{H}\epsilon_n \\ &= -\lambda\epsilon_n \\ \frac{\|\epsilon_{n+1}\|}{\|\epsilon_n\|} &= \|\mathbf{I} - \lambda\|dt/\xi \end{aligned} \quad (\text{A4})$$

where λ is a matrix containing all eigenvalues of \mathbf{H} . Enforcing the criteria of stability on the equation above we have,

$$\begin{aligned} \frac{\|\epsilon_{n+1}\|}{\|\epsilon_n\|} &\leq 1 \\ \|\mathbf{I} - \lambda\|dt/\xi &\leq 1 \\ 0 &\leq \|\lambda_{max}\|dt/\xi \leq 2 \end{aligned} \quad (\text{A5})$$

where λ_{max} is the largest eigenvalue for \mathbf{H} . Since all eigenvalues would be real for this physical system, we now have,

$$\begin{aligned} 0 &\leq \|\lambda_{max}\|dt/\xi \leq 2 \\ dt &\leq 2\xi/\lambda_{max} \end{aligned} \quad (\text{A6})$$

For most configurations, explored in our system simulation the λ_{max} varies around $\sim 1-10$. This gives us that $dt \leq \xi/5$ is the condition for stability. Here, we choose $dt = \xi/10$, as the step size for all simulations reported in this study. Since we have Eq. 3, which also controls overall dynamics, this choice of time-step was validated for convergence. We have verified that our explicit Euler scheme was converged by checking other smaller values of dt . Other schemes like the RK-2 also produced similar results. Further, for $\xi > 0.01$, we stuck with the use of $dt = 0.001$, as the system moves further away from mechanically stable states and the above approximation in Eq. A3 fails to strictly hold.

3. Dimensionless group analysis: Deborah number

Apart from evaluating the *Deborah number* De as the ratio of the damped relaxation time from Eq. 2 ($\tau_R = \xi\langle a \rangle^2/\epsilon$) and probing time associated with changing bubble radii (a) imparted by the coarsening process, Eq. 3 ($\tau_C = \langle a \rangle^2/\alpha_1$), we can do a simple Buckingham Pi analysis to determine the relevant Π group. Below, we present the analysis to derive the Deborah number as a Π group.

One can re-model the system through an experimental lens and pose the problem statement as measuring the average radii (a) as a function of time. Intuitively, this might be influenced by system properties like ϵ , ρ , α_1 , ξ . These 4 quantities along with $\langle a \rangle$, are comprised of the dimensions M , L and T . Thus 2 Π groups can be made using these variables for every combination of 3 repeating variables being chosen. Here, we choose ρ , α , and ξ as are repeating variables.

$$\begin{aligned} \Pi_1 &= f(\epsilon, \rho, \alpha_1, \xi) \\ &= \epsilon\rho^x\alpha_1^y\xi^z \end{aligned} \quad (\text{A7})$$

Solving for x , y , and z so that Π_1 is dimensionless, we get $\Pi_1 = \epsilon/(\alpha_1\xi)$ or $De = \xi\alpha_1/\epsilon$.

Appendix B: Rheology

1. Analytical Derivation

Here, we provide a derivation for the integral equation Eq. 7, which we used to compute the viscoelastic moduli for our simulation. We start by noting that the theory of viscoelasticity for linear materials [25, 26] shows that the creep compliance J , can be related to the stress σ and strain γ as follows:

$$\int_{-\infty}^t J(t-t')\dot{\sigma}(t')dt' = \gamma(t) \quad (\text{B1})$$

Here we may note that J , σ and γ are $= 0 \forall t \in (-\infty, 0)$ and $\geq 0 \forall t \in [0, \infty)$. Thus, we can extend the integral limits by doing the following:

$$\begin{aligned} \int_{-\infty}^{\infty} J(t-t')\dot{\sigma}(t-t')dt' &= \gamma(t) \\ \int_{-\infty}^{\infty} \dot{J}(t-t')\sigma(t-t')dt' &= \gamma(t) \end{aligned} \quad (\text{B2})$$

using the product rule

$$\int_0^t \dot{J}(t-t')\sigma(t-t')dt' + J(0)\sigma(t) = \gamma(t)$$

Taking the Fourier Transform of the non-decomposed equation above and applying the convolution theorem gives us,

$$\tilde{J} \tilde{\sigma} = \tilde{\gamma} \quad (\text{B3})$$

While one could potentially work with Eq. B2 or Eq. B3, the numerical inaccuracies associated with an FT [13, 20] and the statistical noise in a trajectory function like $\sigma(t)$ or $\gamma(t)$, would make the procedure more difficult. Thus, we use the Wiener-Khinchin theorem and further transform the auto-correlation into its mean squared version as follows:

$$\begin{aligned} \tilde{J} \tilde{J} &= \frac{\|\tilde{\gamma}\|^2}{\|\tilde{\sigma}\|^2} \\ &= \frac{\widetilde{R_{\gamma\gamma}}}{\widetilde{R_{\sigma\sigma}}} \\ &= \frac{\langle \gamma^2 \rangle - \langle \Delta\gamma^2 \rangle / 2}{\langle \sigma^2 \rangle - \langle \Delta\sigma^2 \rangle / 2} \end{aligned} \quad (\text{B4})$$

Reshuffling this equation and taking the inverse FT yields an integral equation. We decompose the limits to stay between 0 and t , which adds a few boundary terms for the step function jump in J and σ at $t = 0$. Further,

we change our notation for t to τ , to be consistent with the MSDs which are calculated as averages over lag times.

$$\begin{aligned} 2J^2(0)\langle \sigma^2 \rangle + \int_0^\tau f(\tau-t')(\langle \sigma^2 \rangle - \langle \Delta\sigma^2 \rangle(t')/2)dt' \\ = (\langle \gamma^2 \rangle - \langle \Delta\gamma^2 \rangle(\tau)/2) \end{aligned} \quad (\text{B5})$$

where $f(\tau)$ is defined as follows,

$$f(\tau) = \left(\int_0^\tau \dot{J}(\tau-t'')\dot{J}(t'')dt'' + 2J(0)\dot{J}(\tau) \right)$$

This equation can be approximated, using similar mathematical approximations as used earlier in Ref. [20].

$$\begin{aligned} \int_0^\tau g(\tau-t')\langle \Delta\sigma^2 \rangle(t')dt' = \langle \Delta\gamma^2 \rangle(\tau) \\ \text{where } g(\tau) \text{ is defined as follows,} \end{aligned} \quad (\text{B6})$$

$$g(\tau) = \left(\int_0^\tau \dot{J}(\tau-t'')\dot{J}(t'')dt'' \right)$$

We approximate the right-hand side of this equation using the bubble portions \mathbf{r} [19, 24], giving: $\simeq 3\pi\langle a \rangle (\langle \mathbf{r}^2 \rangle - \langle \Delta\mathbf{r}^2 \rangle(\tau_i)/2) / \langle a \rangle^3$. However, it may be noted that this equation is not well defined at $\tau = 0$. Thus we evaluate this only for lag times greater than zero. To get an accurate solution, we consider the above equation at various finite lag time values or τ_i and solve a set of simultaneous equations to find the appropriate creep compliance, $J(t)$. Specifically, we choose $\tau_i \in \{\tau_1, \tau_2, \tau_3 \dots \tau_{max}\}$. Here, τ_1 can be as small as dt . We report here results for $\tau_1 = 1$. This choice, however, brings in some numerical error due to the integrals going from $0 \rightarrow \tau$. It may be noted that this equation is mathematically exact for $\forall \tau > 0$ and that the upper limit of our observation $-\tau_{max}$, does not affect the numerical procedure, effectively avoiding a source of truncation error present in many earlier approaches.

2. Choice of Fitting Model

One may notice that solving Eq. B5 or Eq. B6 requires a model for $J(t)$. Here we choose a modified version of the model suggested in Ref. [8]. The original model put forth in the above study has a terminal mode of relaxation at long times, given by t/η_R , and has been observed previously in experiments [10]. In our simulations, we, however, do not observe any terminal relaxation and thus ignore the additional term mentioned above. We considered a modified version of the model given as follows.

$$J(t) = 1/G_\infty + k_D/G_\infty[(1+t/\tau_0)^\beta - 1] \quad (\text{B7})$$

-
- [1] P. Sollich, F. Lequeux, P. Hébraud, and M. E. Cates, Rheology of soft glassy materials, *Physical Review Letters* **78**, 2020–2023 (1997).
- [2] P. Sollich, Rheological constitutive equation for a model of soft glassy materials, *Physical Review E* **58**, 738–759 (1998).
- [3] P. Hébraud and F. Lequeux, Mode-coupling theory for the pasty rheology of soft glassy materials, *Physical Review Letters* **81**, 2934–2937 (1998).
- [4] P. Bursac, G. Lenormand, B. Fabry, M. Oliver, D. A. Weitz, V. Viasnoff, J. P. Butler, and J. J. Fredberg, Cytoskeletal remodelling and slow dynamics in the living cell, *Nature Materials* **4**, 557–561 (2005).
- [5] B. D. Hoffman, G. Massiera, K. M. V. Citters, and J. C. Crocker, The consensus mechanics of cultured mammalian cells, *Proceedings of the National Academy of Sciences* **103**, 10259–10264 (2006).
- [6] B. D. Hoffman and J. C. Crocker, Cell mechanics: Dissecting the physical responses of cells to force, *Annual Review of Biomedical Engineering* **11**, 259–288 (2009).
- [7] A. Ikeda, L. Berthier, and P. Sollich, Unified study of glass and jamming rheology in soft particle systems, *Phys. Rev. Lett.* **109**, 018301 (2012).
- [8] F. A. Lavergne, P. Sollich, and V. Trappe, Delayed elastic contributions to the viscoelastic response of foams, *The Journal of Chemical Physics* **156**, 154901 (2022), <https://doi.org/10.1063/5.0085773>.
- [9] K. Rodriguez-Cruz, M. Molaei, A. Thirumalaiswamy, C. Feitosa, V. N. Manoharan, S. Sivarajan, D. H. Reich, R. A. Riggleman, and J. C. Crocker, Fractal landscape dynamics in dense emulsions and stock prices (2022).
- [10] A. D. Gopal and D. J. Durian, Relaxing in foam, *Phys. Rev. Lett.* **91**, 188303 (2003).
- [11] D. J. Durian, Foam mechanics at the bubble scale, *Physical Review Letters* **75**, 4780–4783 (1995).
- [12] D. J. Durian, Bubble-scale model of foam mechanics: Melting, nonlinear behavior, and avalanches, *Physical Review E* **55**, 1739–1751 (1997).
- [13] H. J. Hwang, R. A. Riggleman, and J. C. Crocker, Understanding soft glassy materials using an energy landscape approach, *Nature Materials* **15**, 1031–1036 (2016).
- [14] A. Gopal and D. J. Durian, Nonlinear bubble dynamics in a slowly driven foam, *Physical Review Letters* **75**, 2610 (1995).
- [15] R. Höhler, S. Cohen-Addad, and A. Asnacios, Rheological memory effect in aqueous foam, *Europhysics Letters* (EPL) **48**, 93 (1999).
- [16] I. K. Ono, S. Tewari, S. A. Langer, and A. J. Liu, Velocity fluctuations in a steadily sheared model foam, *Phys. Rev. E* **67**, 061503 (2003).
- [17] P. Stevenson, Inter-bubble gas diffusion in liquid foam, *Current Opinion in Colloid & Interface Science* **15**, 374 (2010).
- [18] S. Tewari, D. Schiemann, D. J. Durian, C. M. Knobler, S. A. Langer, and A. J. Liu, Statistics of shear-induced rearrangements in a two-dimensional model foam, *Phys. Rev. E* **60**, 4385 (1999).
- [19] A. W. C. Lau, B. D. Hoffman, A. Davies, J. C. Crocker, and T. C. Lubensky, Microrheology, stress fluctuations, and active behavior of living cells, *Phys. Rev. Lett.* **91**, 198101 (2003).
- [20] J. C. Crocker and B. D. Hoffman, Multiple-particle tracking and two-point microrheology in cells, *Methods in Cell Biology Cell Mechanics*, 141–178 (2007).
- [21] C. S. O’Hern, S. A. Langer, A. J. Liu, and S. R. Nagel, Random packings of frictionless particles, *Phys. Rev. Lett.* **88**, 075507 (2002).
- [22] K. Feitosa, O. L. Halt, R. D. Kamien, and D. J. Durian, Bubble kinetics in a steady-state column of aqueous foam, *Europhysics Letters* **76**, 683 (2006).
- [23] A. J. Liu and S. R. Nagel, Jamming is not just cool any more, *Nature* **396**, 21–22 (1998).
- [24] T. G. Mason, Estimating the viscoelastic moduli of complex fluids using the generalized stokes-einstein equation, *Rheologica Acta* **39**, 371 (2000).
- [25] V. Volterra, Sulle equazioni integro-differenziali della teoria dell’ elasticita, *Atti Reale Accad. naz. Lincei. Rend. Cl. sci. fis., mat. e natur.* **18**, 295 (1909).
- [26] V. Volterra and P. Joseph, *Leçons sur les fonctions de lignes: Professés a la sorbone en 1912* (Gauthier-Villars, 1913).
- [27] G. C. Rossi and M. Testa, The stress tensor in thermodynamics and statistical mechanics, *The Journal of Chemical Physics* **132**, 074902 (2010).
- [28] M. Zhou, A new look at the atomic level virial stress: on continuum-molecular system equivalence, *Proceedings of the Royal Society of London. Series A: Mathematical, Physical and Engineering Sciences* **459**, 2347 (2003).
- [29] E. Bitzek, P. Koskinen, F. Gähler, M. Moseler, and P. Gumbsch, Structural relaxation made simple, *Phys. Rev. Lett.* **97**, 170201 (2006).